

Cite this: *Mater. Adv.*, 2022,
3, 290

Electronic structure of $\text{Li}^+\text{@C}_{60}$ adsorbed on methyl-ammonium lead iodide perovskite $\text{CH}_3\text{NH}_3\text{PbI}_3$ surfaces†

Khian-Hooi Chew,^a Riichi Kuwahara^b and Kaoru Ohno^c

It was recently shown by Jeon *et al.* [*Angew. Chem.*, 2018, **57**, 4607] that air stability for more than 1000 hours under light illumination can be achieved in methyl-ammonium (MA) lead iodide perovskite solar cells when Li^+ is replaced by $\text{Li}^+\text{@C}_{60}$ in a dopant material used in the p-type donor layer. In order to demonstrate the role of $\text{Li}^+\text{@C}_{60}$ in the hole transporting material, we carried out first-principles electronic structure calculations of $\text{Li}^+\text{@C}_{60}$ adsorbed on MAPbI_3 using the van der Waals corrected density functional theory. We used finite slab models of tetragonal MAPbI_3 (001) surfaces with MAI terminations. Using the most stable MAPbI_3 surfaces, we introduced one $\text{Li}^+\text{@C}_{60}$ molecule on various positions of the MAI surface and performed geometrical optimizations. Then, we found that the $\text{Li}^+\text{@C}_{60}$ was adsorbed at the aboveC position with almost 100% ionization. There is not much difference between the top and bottom positions of Li^+ inside C_{60} , but the bottom position is slightly more stable than the top position. In the $\text{MAPbI}_3/\text{Li}^+\text{@C}_{60}$ system, the Kohn–Sham (KS) wave functions of the HOMO and HOMO-1 levels are spread out in MAPbI_3 and those of the LUMO, LUMO+1, LUMO+2 levels are localized in $\text{Li}^+\text{@C}_{60}$; the energy gap between these levels is 0.6 eV. Thus, in the neutral, spin-polarized $\text{MAPbI}_3/\text{Li}^+\text{@C}_{60}$ system, the KS wave functions of the HOMO (SOMO, – spin) and LUMO (+spin) levels are both localized in $\text{Li}^+\text{@C}_{60}$ and their energy gap of 0.125 eV is very small. This HOMO (SOMO) level behaves as a hole level when it loses an electron to become $\text{Li}^+\text{@C}_{60}$. Since there are three almost degenerate LUMO+1 and LUMO+2 levels, it is expected to behave as a good hole conductor. As such, we conclude that the use of $\text{Li}^+\text{@C}_{60}$ molecules in place of the bare Li-ions as dopant materials in the MAPbI_3 solar cells can prevent degradation. In any case, regardless of the adsorption geometry, our results clearly show the existence of the energetically isolated hole level localized in the $\text{Li}^+\text{@C}_{60}$, which may successfully contribute to the suppression of the oxidation of the MAPbI_3 surface.

Received 19th August 2021,
Accepted 12th October 2021

DOI: 10.1039/d1ma00741f

rsc.li/materials-advances

Introduction

Methylammonium (MA) lead halide perovskites such as $\text{CH}_3\text{NH}_3\text{PbI}_3$ (hereafter abbreviated to MAPbI_3) have attracted significant attention since the discovery of the efficient photovoltaic behaviour of the heterojunction of MAPbI_3 and TiO_2 by Miyasaka's group in 2009.^{1–3} So far, various heterojunction systems overlaid with SnO_2 , C_{60} , C_{60} derivatives like PCBM, and so on have been proposed by many researchers, and the light-current energy conversion efficiency has rapidly increased from 3.8%¹ to over 20%.^{3–7} In a typical architecture of

perovskite solar cells (PSCs), MAPbI_3 works as a photo-absorber and is sandwiched by an n-type acceptor layer and a p-type donor layer. The former is made of electron transporting material (ETM) such as C_{60} and C_{60} derivatives and the latter is made of hole transporting material (HTM) such as 2,2',7,7'-tetrakis(*N,N*-di-*p*-methoxyphenylamine)-9,9'-spirobi-fluorene (spiro-MeOTAD) and poly(3,4-ethylenedioxythiophene) polystyrene sulfonate (PEDOT:PSS).^{2,8–11}

Although the application of Spiro-MeOTAD as an HTM in PSCs^{2,12} has been an important step in improving the energy conversion efficiency, the low long-term stability under light illumination and the coexistence of oxygen and water have been serious drawbacks of PSCs for commercial use.^{13–15} In particular, the dopants used in the HTM suffer from degradation.^{13–17} In order to reduce degradation, Jeon *et al.*¹⁸ proposed the use of Li-ion encapsulated C_{60} ($\text{Li}^+\text{@C}_{60}$) instead of bare Li-ions (Li^+) in combination with bis(trifluoromethanesulfonyl)imide (TFMSI[–]) as a p-type dopant. Using this dopant, they reported

^a Department of Physics, University of Malaya, 50603 Kuala Lumpur, Malaysia.
E-mail: khchew@um.edu.my

^b Dassault Systèmes, ThinkPark Tower, 2-1-1 Osaki, Shinagawa-ku, Tokyo 141-6020, Japan

^c Department of Physics, Yokohama National University, 79-5 Tokiwadai, Hogogaya-ku, Yokohama 240-8501, Japan

† Electronic supplementary information (ESI) available. See DOI: 10.1039/d1ma00741f



that spiro-MeOTAD⁺TFSI⁻ functions as an effective HTM and Li⁺@C₆₀ functions as an antioxidant, reacting with intruding oxygen. By preventing unnecessary oxidation in the device system, the [Li⁺@C₆₀]TFSI⁻ device achieved a stability of approximately 7-fold that of conventional Li⁺TFSI⁻ devices in MAPbI₃-based PSCs, and 10-fold that of a more stable mixed ion lead halide PSCs. Consequently, the passivated PSCs showed no decrease in the energy conversion efficiency for more than 1000 hours while being continuously illuminated under ambient conditions.

Atomistic modelling and simulation based on first-principles density functional theory (DFT) can play an important role in revealing the underlying mechanisms of the high performance of PSCs.^{19–21} Yin *et al.*²² studied the energy alignment and charge transfer properties at the interface between MAPbI₃, perovskites and Spiro-MeOTAD and PCBM. They found that the MAPbI₃ (001) and (110) surfaces favored hole injection to the hole acceptor Spiro-MeOTAD, whereas the polar MAPbI₃ (001) surface facilitated electron transfer to the PCBM. However, concerning the reduction of the degradation of PSCs, the role of Li⁺@C₆₀ adsorbed on the MAPbI₃ surface in the experiment by Jeon *et al.*¹⁸ remains unclear. Therefore, the purpose of this paper is to investigate the electronic structure of Li⁺@C₆₀ adsorbed on the MAPbI₃ surface. The mass production of Li⁺@C₆₀ was achieved by a plasma shower method,²³ which was suggested by a first-principles molecular dynamics study²⁴ and experiments.^{25,26} The maximum production ratio in this method was theoretically estimated to be about 3.7%.²⁷ Now, Li⁺@C₆₀ has the potential for many applications.^{28–33}

Computational methods

First-principles all-electron calculations were performed by using the DMol³ package,^{34–36} which adopts numerical atomic orbitals. A standard DFT dispersion (DFT-D) correction was employed to take into account van der Waals interactions³⁷ in the Tkatchenko-Scheffler (TS) scheme.³⁸ This method is formally identical to the DFT-D2 method of Grimme but the dispersion coefficients and damping function are charge-density dependent. The DFT-TS method can therefore handle the change in the vdW contribution of atoms due to their chemical environment. In the present study, we considered a slab model of the tetragonal phase of MAPbI₃ (001) with MAI-terminated surfaces. The slab model has a 2 × 2 periodicity in-plane and is four MAI-layers thick, with the assumption of 50 Å vacuum regions between the slabs, which are large enough to avoid the interactions between periodic images. The MAPbI₃ slab model and endohedral Li⁺@C₆₀ fullerene were first optimized to achieve the minimum energy. We introduced one Li⁺@C₆₀ molecule on the MAPbI₃ (001) layer, forming a hybrid MAPbI₃/Li⁺@C₆₀ structure with a total of 445 atoms. For the MAPbI₃/Li⁺@C₆₀ interface, the dipole slab correction for the electrostatic potential was taken into account in the calculations due to the existence of polar bonds.

All calculations (except for perovskites with bare surfaces) were performed based on the spin unrestricted (*i.e.*, spin-polarized) approach using the generalized gradient approximation (GGA) in the Perdew–Burke–Ernzerhof (PBE) form for the exchange–correlation functional.³⁹ We have ignored spin-orbit coupling (SOC) because the PBE functional can provide a reasonable estimation of structural, electronic, and optical properties.^{40–42} The double-numerical quality basis, *i.e.*, double numerical plus polarization (DNP) function, was employed for all calculations. The size of these DNP basis sets is comparable to that of the Gaussian 6-31G**. In the calculation, the geometrical optimization was performed with the Fermi smearing of 0.005 Hartree. The tolerances of the energy, gradient, and displacement convergences were set at 1 × 10⁻⁵ Ha, 2 × 10⁻³ Ha Å⁻¹, and 5 × 10⁻³ Å, respectively.

Results & discussion

MAPbI₃ undergoes a structural phase transition from a cubic to a tetragonal phase at ~330 K, and it becomes an orthorhombic structure at temperatures below 160 K.⁴³ In the present study, the room temperature tetragonal phase of MAPbI₃ was chosen as the model structure for studying the structural and electronic properties in the Li@C₆₀ adsorbed geometries. The computationally optimized cell parameters for the bulk tetragonal phase of MAPbI₃ are *a* = 8.70 Å, *b* = 8.72 Å and *c* = 12.83 Å, which are comparable to experimental values.^{43,44} A typical PSC has asymmetric interfaces ETM/MAPbI₃/HTM. Therefore, we consider an asymmetric slab model with the MAI as the top surface layer (facing the vacuum layer) and the PbI layer as the bottom layer of MAPbI₃. Here, the MAI-terminated surface is set as the MAPbI₃ top surface because this surface facilitates the electron transfer to the C₆₀ ETM.⁴⁵

Many studies have shown that the MA orientation plays an important role in governing the stability and electronic structures of MAPbI₃.^{7,42,45–48} The orientation of the MA molecule

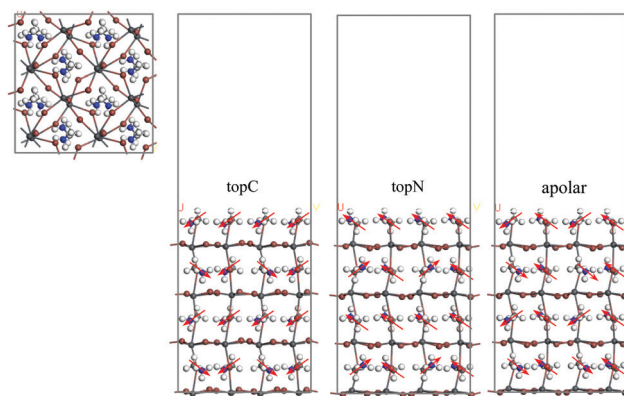


Fig. 1 Slab models constructed for the simulation of the MAPbI₃ (001) surfaces with MAI terminations: top and side views of tetragonal MAPbI₃ (001) surfaces for topC, topN and apolar geometries. The red arrows show the molecular dipole of a MA cation with the NH₃ group as the arrowhead. White, light grey, blue, brown, and dark grey spheres represent the H, C, N, I, and Pb atoms, respectively.



Table 1 Valence band edge (VBE), conductance band edge (CBE), band gap and the total relative energies of the bare-surface for tetragonal MAPbI₃ perovskites

MA orientation	VBE [eV]	CBE [eV]	Band gap [eV]	Total energy relative to the topC [eV]
topC	-5.371	-3.888	1.482	0.00
topN	-4.644	-3.552	1.092	3.814
Apolar	-4.905	-3.619	1.286	2.505
Experiment			1.55 ^a	

^a Ref. 45.

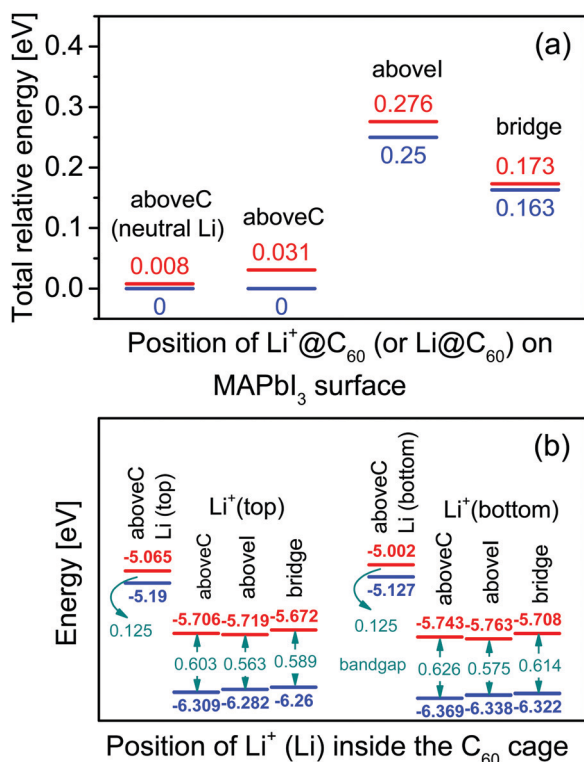


Fig. 2 (a) Total energy of a tetragonal MAPbI₃ with a Li⁺@C₆₀ (a Li@C₆₀) relative to the aboveC position. The Li⁺ (Li) is located at the off-central top (— red line) and bottom (— blue line) positions inside the C₆₀ cage. The total energy of a MAPbI₃ with a neutral lithium endohedral fullerene Li@C₆₀ was calculated only for the aboveC position. (b) The highest occupied molecular orbital (— HOMO), lowest unoccupied molecular orbital (— LUMO) and band gap of the tetragonal MAPbI₃ with a Li⁺@C₆₀ on the aboveC, above, and bridge positions. The MAPbI₃ with a neutral lithium endohedral fullerene Li@C₆₀ was calculated only for the aboveC position.

has a significant effect on the charge mobility,⁴⁶ the bandgap change⁴⁷ and photo-energy conversion efficiencies.^{7,48} Neutron scattering measurements suggested the formation of either antiferroelectric or ferroelectric domains in these perovskites based on the ordered orientation of MA cations.⁴⁸ However, the highly disordered orientation of the MA cation at room temperature excludes the possibility of spontaneous polarization in the antiferroelectrics or ferroelectrics due to the ordered orientation of MA cations. In order to take into account the MA orientation effect, we considered three orientations of the MA

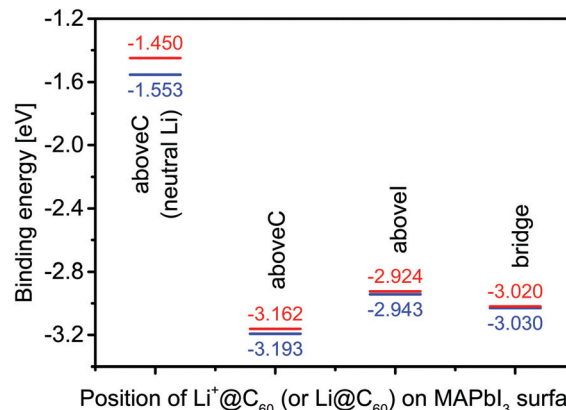


Fig. 3 The binding energy of a tetragonal MAPbI₃ with a Li⁺@C₆₀ (a Li@C₆₀). The Li⁺ (Li) is located at the off-central top (— red line) and bottom (— blue line) positions inside the C₆₀ cage. The calculated binding energy of a MAPbI₃ with a neutral lithium endohedral fullerene Li@C₆₀ is only for the aboveC position.

cation with respect to the top surface as shown in Fig. 1: (i) the topC model with the CH₃ group pointing up in all layers, (ii) the topN model with the NH₃ group pointing up in all layers, and (iii) the apolar model with half of -NH₃ or -CH₃ groups

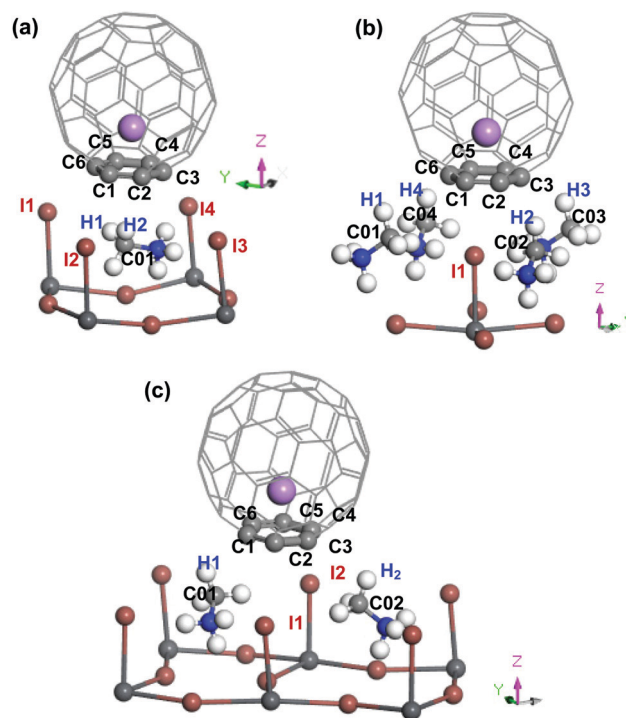


Fig. 4 Perspective view (only selected area at the interface between MAPbI₃ and Li⁺@C₆₀) of the topC-oriented MAPbI₃ with a lithium endohedral fullerene Li⁺@C₆₀ on the (a) aboveC, (b) above and (c) bridge position. The Li⁺ is located at the off-central bottom inside the C₆₀ cage. H, C, N, I, Pb and Li atoms are represented by the white, light grey, blue, brown, dark grey and purple spheres, respectively. Atoms located at the interface between MAPbI₃ and C₆₀ are labelled, and their atomic distances within the estimated vdWs atomic radius are summarized in Table 2.



pointing up and half pointing down. We first looked at the energetics of the slab models. In Table 1, we summarize the valence band edge (VBE), conduction band edge (CBE), band gap, and the total relative energies of the tetragonal MAPbI₃ perovskites with the bare surface. The calculated VBE and CBE for the bare-surface tetragonal MAPbI₃ were -4.66 to -5.37 eV and -3.55 to -3.88 eV, respectively. Among them, the topC orientation was the most stable structure with the bandgap of 1.48 eV, in agreement with other works.⁴⁹ Since the topC model is the most stable structure, we will focus on the tetragonal MAPbI₃ perovskites with the topC orientation by introducing a Li⁺@C₆₀ molecule on various MAPbI₃ surfaces: the aboveC, aboveI and bridge positions (see Fig. S1–S3 of the ESI[†]). In each case, we examined the effect of the Li⁺ located at the off-central top and bottom inside the C₆₀ cage on the electronic structures of the MAPbI₃/Li⁺@C₆₀ system. Hereafter, we denote the Li⁺(top)@C₆₀ and Li⁺(bottom)@C₆₀ molecules as the lithium-ion endohedral fullerene with the Li⁺ located at the off-central “top” and “bottom” inside the C₆₀ cage, respectively.

Using the most stable topC model, we introduced one Li⁺@C₆₀ molecule on the aboveC, aboveI and bridge positions of the MAI surface and performed geometrical optimizations. Fig. 2(a) shows the total energy of the MAPbI₃/Li⁺@C₆₀ system relative to the case with a Li⁺(bottom)@C₆₀ on the aboveC geometry. The corresponding HOMO, LUMO and band gap are shown in Fig. 2(b). The binding energy of the MAPbI₃/Li⁺@C₆₀ system for three different geometries and the binding energy of the MAPbI₃/Li@C₆₀ system for the aboveC geometry are shown in Fig. 3. In general, the stability of the MAPbI₃/Li⁺@C₆₀ system is in the order of a Li⁺@C₆₀ on the aboveC > bridge > aboveI position. From Fig. 3, the binding energy of the MAPbI₃/Li@C₆₀ system also increased in the order of a Li⁺@C₆₀ on the aboveC > bridge > aboveI geometry, which further confirmed the stability of the MAPbI₃/Li⁺@C₆₀ system. In addition, the MAPbI₃/Li⁺(bottom)@C₆₀ system is energetically more stable than the MAPbI₃/Li⁺(top)@C₆₀ system for the same geometry (see Fig. 2(a)), which is also consistent with the binding energies of the MAPbI₃/Li⁺@C₆₀ system

Table 3 Hirshfeld atomic charges of fragments [CH₃] and [I] at the MAPbI₃/Li⁺@C₆₀ interface with the Li⁺@C₆₀ on the aboveC, aboveI and bridge positions. [Li⁺@C₆₀] and [MAPbI₃] denote the calculated Hirshfeld fragments of the MAPbI₃/Li⁺@C₆₀ system. Q is the charge transferred from [MAPbI₃] to [Li⁺@C₆₀]. The Li⁺ is located at the off-central top (Li⁺/Li(top)) and bottom (Li/Li⁺(bottom)) inside the C₆₀ cage. Fragments [CH₃] and [I] are labelled according to Fig. 4. Calculated Hirshfeld atomic charges of a MAPbI₃ with a neutral lithium endohedral fullerene Li@C₆₀ are for only the aboveC position

Atom/ molecule	Surface geometry					
	aboveC [e]		aboveI [e]		Bridge [e]	
	Li (top)	Li (bottom)	Li ⁺ (top)	Li ⁺ (bottom)	Li ⁺ (top)	Li ⁺ (bottom)
[C01H ₃]	-0.004	-0.007	0.057	0.058	0.058	0.057
[I1]	-0.205	-0.211	-0.169	-0.177	-0.213	-0.218
[Li ⁺ @C ₆₀]	0.208	0.239	0.245	0.271	0.248	0.278
[MAPbI ₃]	0.789	0.758	0.752	0.726	0.745	0.715
MAPbI ₃ / Li ⁺ @C ₆₀	0.997	0.997	0.997	0.997	0.993	0.994
Q	-0.794	-0.763	-0.757	-0.731	-0.750	-0.720
[C01H ₃]	-0.006	-0.007				
[I1]	-0.212	-0.211				
[Li@C ₆₀]	-0.049	-0.067				
[MAPbI ₃]	0.046	0.064				
MAPbI ₃ / Li@C ₆₀	-0.003	-0.003				
Q	-0.051	-0.069				

(see Fig. 3)). Although iodine has a high electronegativity, a Li⁺@C₆₀ adsorbed on the aboveI position of the CH₃NH₃PbI₃ surface is energetically less favorable as compared to other geometries. Among the MAPbI₃/Li⁺@C₆₀ systems, a Li⁺(bottom)@C₆₀ adsorbed on the aboveC geometry of the MAPbI₃ surface is the most stable structure with the strongest binding energy of -3.193 eV (Fig. 3) and the highest bandgap value of 0.626 eV (Fig. 2(b)).

For the MAPbI₃/Li⁺(bottom)@C₆₀ system, the LUMO varies from -5.708 eV to -5.763 eV and the HOMO has a value range from -6.322 eV to -6.369 eV, leading to a bandgap value in the range from 0.575 eV to 0.626 eV. Compared with the MAPbI₃/Li⁺(bottom)@C₆₀ system, the MAPbI₃/Li⁺(top)@C₆₀ system has

Table 2 Atomic distances of selected atoms located within the vdWs atomic radius at the MAPbI₃/Li⁺@C₆₀ interface with the Li⁺@C₆₀ on the aboveC, aboveI and bridge positions. Calculated atomic distances at the interface between the MAPbI₃ and a neutral Li endohedral fullerene Li@C₆₀ are for only the aboveC position. The Li⁺/Li is located at the off-central top inside the C₆₀ cage. Values in brackets denote the atomic distance for the Li⁺/Li located at the off-central bottom inside the C₆₀ cage. Atoms are labelled according to Fig. 4

Surface geometry	C···H distance [Å] [vdWs radius < 2.97 Å]	C···C distance [Å] [vdWs radius < 3.54 Å]	C···I distance [Å] [vdWs radius < 3.81 Å]
aboveC (neutral Li)	C5···H1	— (2.944)	
	C1···H2	2.672 (2.967)	C1···C01 3.547 (3.538)
	C2···H2	2.621 (2.618)	C2···C01 3.545 (3.544)
	C3···H2	2.973 (—)	
aboveC	C1···H2	2.665 (2.660)	C1···C01 3.544 (3.538)
	C2···H2	2.619 (2.612)	C2···C01 (3.544)
aboveI			C1···I1 3.411 (3.428)
			C2···I1 3.566 (3.580)
			C3···I1 3.742 (3.742)
			C4···I2 3.762 (3.751)
			C5···I2 3.613 (3.604)
			C6···I2 3.438 (3.442)
bridge	C6···H1	2.801 (2.791)	C2···I1 3.568 (3.519)
	C3···H2	2.990 (2.974)	C5···I2 3.741 (3.703)
			C6···C01 3.457 (3.443)
		C3···C02 3.465 (3.451)	



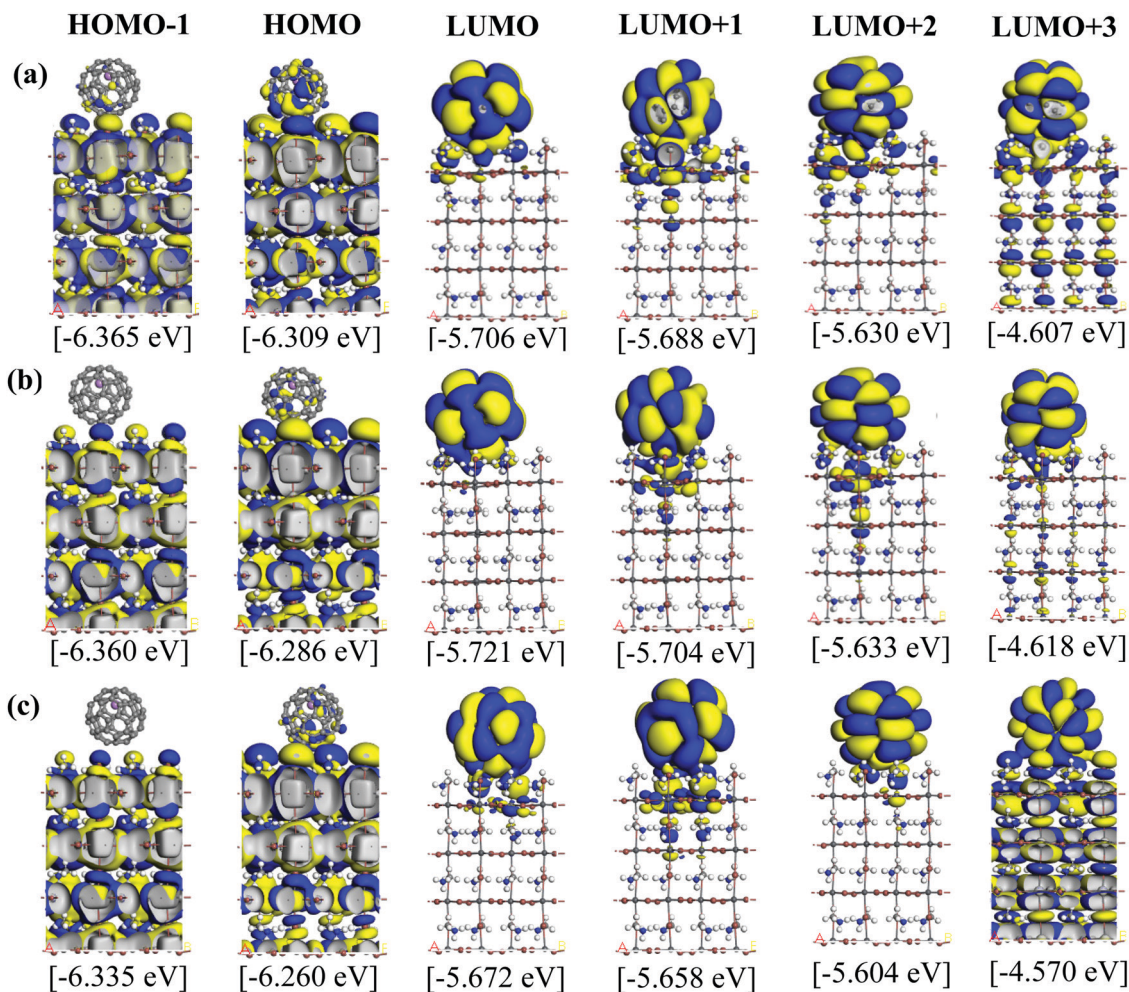


Fig. 5 Calculated KS orbitals and energy eigenvalues of $\text{MAPbI}_3/\text{Li}^+\text{@C}_{60}$ from the HOMO–1 to LUMO+3 levels. The Li^+ is located at the off-central top inside the C_{60} cage. Yellow and blue denote the plus and minus regions of the orbitals. The perovskite has a topC orientation with $\text{Li}^+\text{@C}_{60}$ on the (a) aboveC, (b) aboveI and (c) bridge positions.

a slightly lower bandgap ranging from 0.563 eV to 0.603 eV; the LUMO varies from -5.672 eV to -5.706 eV and the HOMO varies from -6.260 to -6.309 eV. It is interesting to note here that the $\text{MAPbI}_3/\text{Li}^+\text{@C}_{60}$ system with the aboveC (aboveI) geometry has the largest (smallest) bandgap value of 0.603 (0.563) eV and 0.626 (0.575) eV for the Li^+ located at the off-central “top” and “bottom” inside the C_{60} cage, respectively.

Since the $\text{MAPbI}_3/\text{Li}^+\text{@C}_{60}$ system with the aboveC geometry is the most stable structure, we calculated and compared the electronic structures of the $\text{MAPbI}_3/\text{Li}^+\text{@C}_{60}$ system with a neutral lithium endohedral fullerene $\text{Li}\text{@C}_{60}$ absorbed on the aboveC geometry of the MAPbI_3 surface ($\text{MAPbI}_3/\text{Li}\text{@C}_{60}$). The total energy relative to the $\text{MAPbI}_3/\text{Li}(\text{bottom})\text{@C}_{60}$ with the aboveC geometry is depicted in Fig. 2(a), which is very small, *i.e.* ~ 0.008 eV, compared to the $\text{MAPbI}_3/\text{Li}^+\text{@C}_{60}$ system. Since the binding energy of the $\text{MAPbI}_3/\text{Li}\text{@C}_{60}$ system is smaller than that of the $\text{MAPbI}_3/\text{Li}^+\text{@C}_{60}$ system by over 1.5 eV as shown in Fig. 3, $\text{Li}\text{@C}_{60}$ has a great tendency to become a good hole conductor by absorbing a hole. From Fig. 2(b), it is seen that the $\text{MAPbI}_3/\text{Li}(\text{top})\text{@C}_{60}$ has a small band gap of 0.125 eV, which is

independent of the off-central position of Li and is smaller than the bandgap of the $\text{MAPbI}_3/\text{Li}^+\text{@C}_{60}$ system by a factor of 5. The LUMO and HOMO (SOMO) of the $\text{MAPbI}_3/\text{Li}\text{@C}_{60}$ system are ~ -5.0 eV and ~ -5.1 eV, respectively, which are relatively higher than those of the $\text{MAPbI}_3/\text{Li}^+\text{@C}_{60}$ system (see Fig. 7).

When two atoms with opposite charges from two molecular species are in proximity within the sum of their van der Waals (vdW) radii, a non-covalent intermolecular interaction may form between the molecules.^{50–52} At the interface between the $\text{Li}^+\text{@C}_{60}$ (or the $\text{Li}\text{@C}_{60}$) molecule and the topC-oriented MAPbI_3 , the C atoms of C_{60} may interact with the MAPbI_3 surface *via* the I atoms of PbI_3 and H (or C) atoms of MA, as shown in Fig. 4 and Fig. S4–S11 (ESI[†]). The vdW radii of C, H, and I are 1.77 Å, 1.20 Å, and 2.04 Å, respectively.⁵³ This indicates that any $\text{C}\cdots\text{H}(\text{C})$ distance < 2.97 Å, $\text{C}\cdots\text{C}(\text{H3})$ distance < 3.54 Å, or $\text{C}\cdots\text{I}(\text{Pb})$ distance < 3.81 Å may signify a potential interaction between the $\text{Li}^+\text{@C}_{60}$ and MAPbI_3 surface. Based on this criterion, we conducted a simple analysis of the interactions at the $\text{MAPbI}_3/\text{Li}^+\text{@C}_{60}$ interface for three different geometries. We also examined the $\text{MAPbI}_3/\text{Li}\text{@C}_{60}$ system with



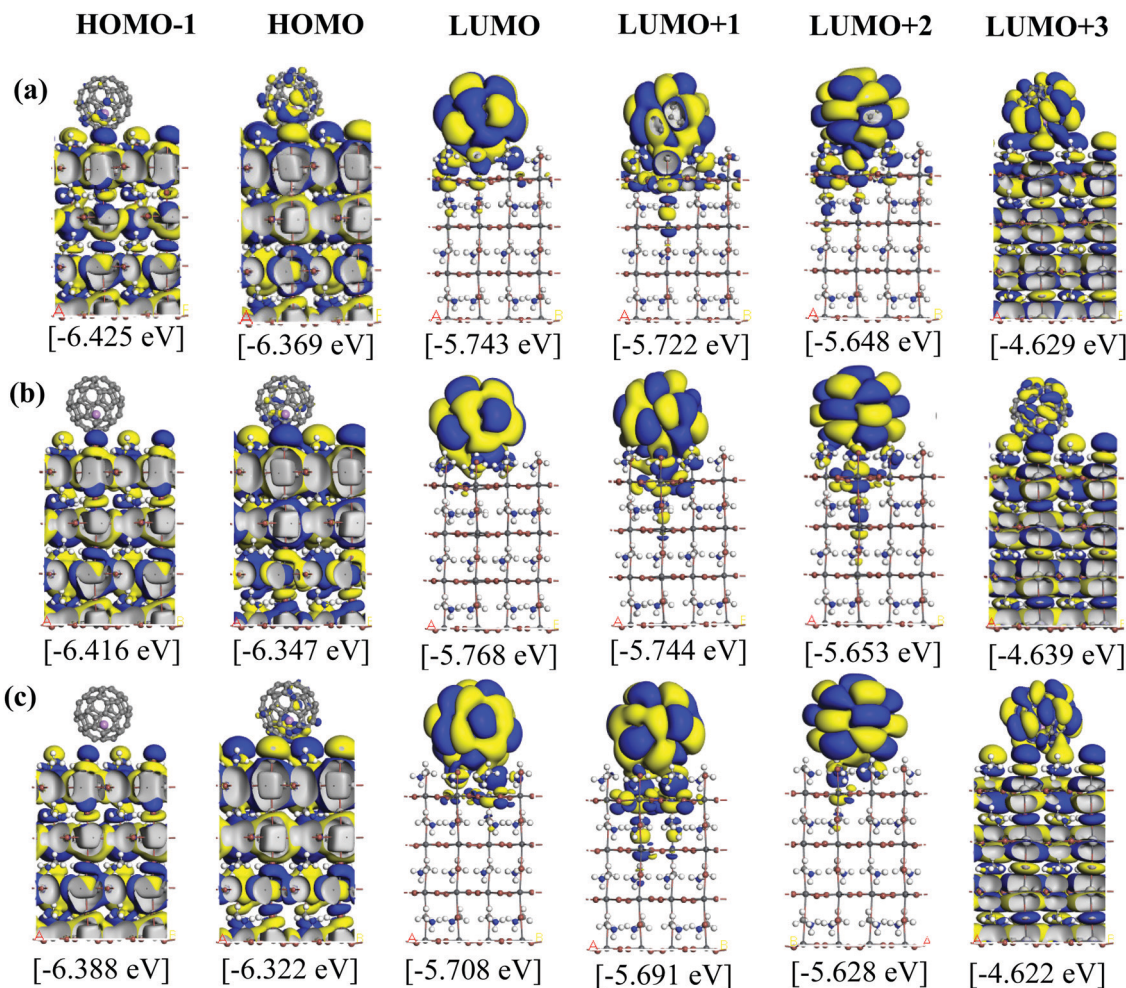


Fig. 6 Calculated KS orbitals and energy eigenvalues of MAPbI₃/Li⁺@C₆₀ from the HOMO–1 to LUMO+3 levels. The Li⁺ located at the off-central bottom inside the C₆₀ cage. Yellow and blue denote the plus and minus regions of the orbitals. The perovskite has a topC orientation with Li⁺@C₆₀ on the (a) aboveC, (b) aboveI and (c) bridge positions.

a neutral lithium endohedral fullerene Li@C₆₀ absorbed on the aboveC geometry of MAPbI₃. In Table 2, we summarize the atomic distance of selected atoms/molecules (fragments) located at the MAPbI₃/Li⁺@C₆₀ interface, as well as the MAPbI₃/Li@C₆₀ interface. A more comprehensive analysis of results can be found in Fig. S4–S11 in the ESI.†

In the following, we correlate the findings in Table 2 with the stability (Fig. 2(a)) and the binding energy (Fig. 3) of the MAPbI₃/Li⁺@C₆₀ system. From Fig. 2(a), we found that the energetically most stable geometry of the MAPbI₃/Li⁺@C₆₀ system is the aboveC geometry and the next stable geometry is the aboveI position. However, both the aboveC and bridge geometries have the C···H(–C), C···C(–H) and C···I(–Pb) interactions. The results from Table 2 show that the main difference between these two geometries is the C···H(–C) atomic distance: the aboveC geometry is in the ranges of 2.612–2.660 Å, whereas it is in the range of 2.791–2.990 Å for the aboveI geometry. This suggests that the C···H(–C) interaction, *i.e.* the π–CH interaction, plays a crucial role in governing the stability of the MAPbI₃/Li⁺@C₆₀ system and the strength of binding between

the MAPbI₃ and Li⁺@C₆₀. The MAPbI₃/Li⁺@C₆₀ system with the aboveI geometry is the least stable structure among the three geometries (though they have six C···I(–Pb) interactions with highly electronegative iodines), implying that the C···I(–Pb) interactions, *i.e.* the π–I interaction, contributed less as compared with the C···H(–C) interactions. All the atomic distances C···H(–C), C···C(–H) and C···I(–Pb) of the MAPbI₃/Li⁺(bottom)@C₆₀ system are shorter than those of the MAPbI₃/Li⁺(top)@C₆₀ system. Therefore, the MAPbI₃/Li⁺(bottom)@C₆₀ system is energetically more stable than the MAPbI₃/Li⁺(top)@C₆₀ system for the structure with the same geometry (Fig. 2(a)). For the same geometry, the binding energy of the MAPbI₃/Li⁺(bottom)@C₆₀ system is also stronger than that of the MAPbI₃/Li⁺(top)@C₆₀ system. Although the MAPbI₃/Li@C₆₀ system has a weak binding energy (Fig. 3), both the MAPbI₃/Li(top)@C₆₀ system and the MAPbI₃/Li(bottom)@C₆₀ system have six bond distances within the vdW interactions (Fig. S4 and S5, ESI†), *i.e.* three C···H(–C) in the range 2.618–2.673 Å, two C···C(–H) in the range 3.538–3.547 Å, and one C···I(–Pb) in the range 3.744–3.782 Å, with a small energy difference of



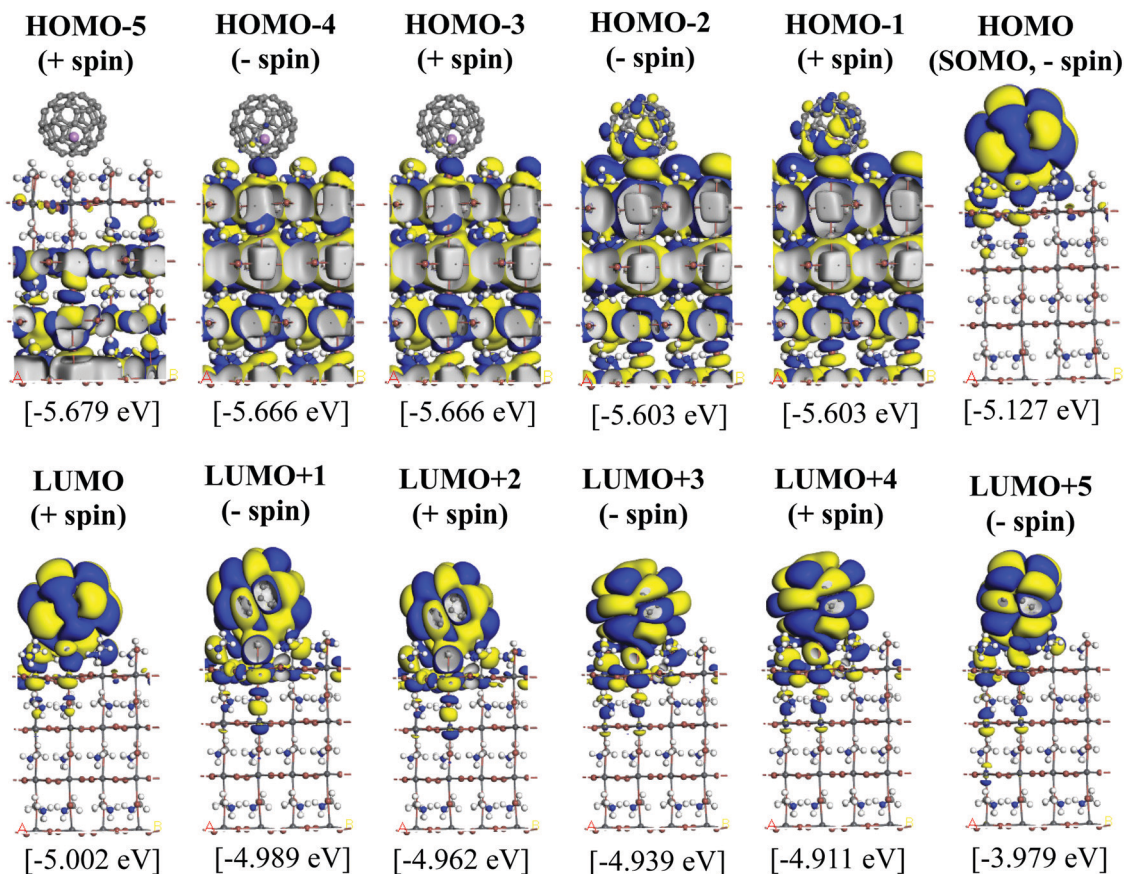


Fig. 7 Calculated KS orbitals and energy eigenvalues of a perovskite MAPbI₃ with a neutral lithium endohedral fullerene Li@C₆₀ on the aboveC position. The Li is located at the off-central bottom inside the C₆₀ cage. Yellow and blue denote the plus and minus regions of the orbitals.

~0.008 eV (Fig. 2(a)). The stability of the Li@C₆₀ molecule is another important factor that contributes to the strength of binding between the MAPbI₃ perovskite and the Li@C₆₀ molecule, besides the atomic distances at the MAPbI₃/Li⁺@C₆₀ interface. Although this simple analysis may provide a rough picture of the interaction at the MAPbI₃/Li⁺@C₆₀ (or Li@C₆₀) interface, it is important to note that the calculated atomic distances using the GGA-PBE may not be accurate. In addition, the lattice dynamics play an important role in determining the structural and electronic properties of these halide perovskites,^{54–56} and the tetragonal structure of MAPbI₃ perovskite at room temperature is strongly anharmonic.⁵⁷

After gaining an understanding of the correlation between the stability and the vdW interactions at the interface, we investigated the atomic charge distribution at the interface between the MAPbI₃ perovskite and Li⁺@C₆₀ (or Li@C₆₀). We performed an atomic charge analysis using the geometrical optimized structure of the MAPbI₃/Li⁺@C₆₀ (and MAPbI₃/Li@C₆₀) system. We employed the Hirshfeld atomic population analysis, which is based on the electron density at individual atoms.^{58,59} The Hirshfeld charges of an individual Li@C₆₀ molecule and the MAPbI₃ slab are 0.0e and -0.005e, respectively, indicating that they possess neutral charges. On the other hand, the calculated Hirshfeld charge of the individual

Li⁺@C₆₀ molecule was 0.998e, ~+1e, as expected. Table 3 summarizes the Hirshfeld atomic charges of selected fragments [CH₃] and [I] at the MAPbI₃/Li⁺@C₆₀ interface. Q is the charge transferred from [MAPbI₃] to [Li⁺@C₆₀]. [Li⁺@C₆₀] and [MAPbI₃] denote the calculated Hirshfeld fragments of the MAPbI₃/Li⁺@C₆₀ system. Calculated Hirshfeld atomic charges of a MAPbI₃ with a neutral lithium endohedral fullerene Li@C₆₀ are for only the aboveC position. A more detailed analysis of the Hirshfeld atomic charges of fragments [CH₃], [I], [Li], [Li⁺], and [C] at the MAPbI₃/Li⁺@C₆₀ interface with the Li⁺@C₆₀ can be found in Table S2 of the ESI.† From Table 3, the MAPbI₃/Li@C₆₀ system also possesses a neutral charge similar to the Hirshfeld charge of the individual Li@C₆₀ molecule and the MAPbI₃ slab, as expected. For the MAPbI₃/Li⁺@C₆₀ system, the calculated Hirshfeld charge for all three geometries including the Li⁺ located at the off-central top and bottom positions inside the C₆₀ cage is ~+1.0e, which is the same as the isolated Li⁺@C₆₀ molecule. In the MAPbI₃/Li⁺@C₆₀ system, the amount of charge transfer Q from the MAPbI₃ to Li⁺@C₆₀ increased in the order of bridge > aboveI > aboveC geometry. The most stable MAPbI₃/Li@C₆₀ system with the aboveC geometry has the highest amount of charge transfer Q, therefore possessing the strongest binding energy. However, the amount of charge transfer of the MAPbI₃/Li⁺@C₆₀ system with the aboveI position



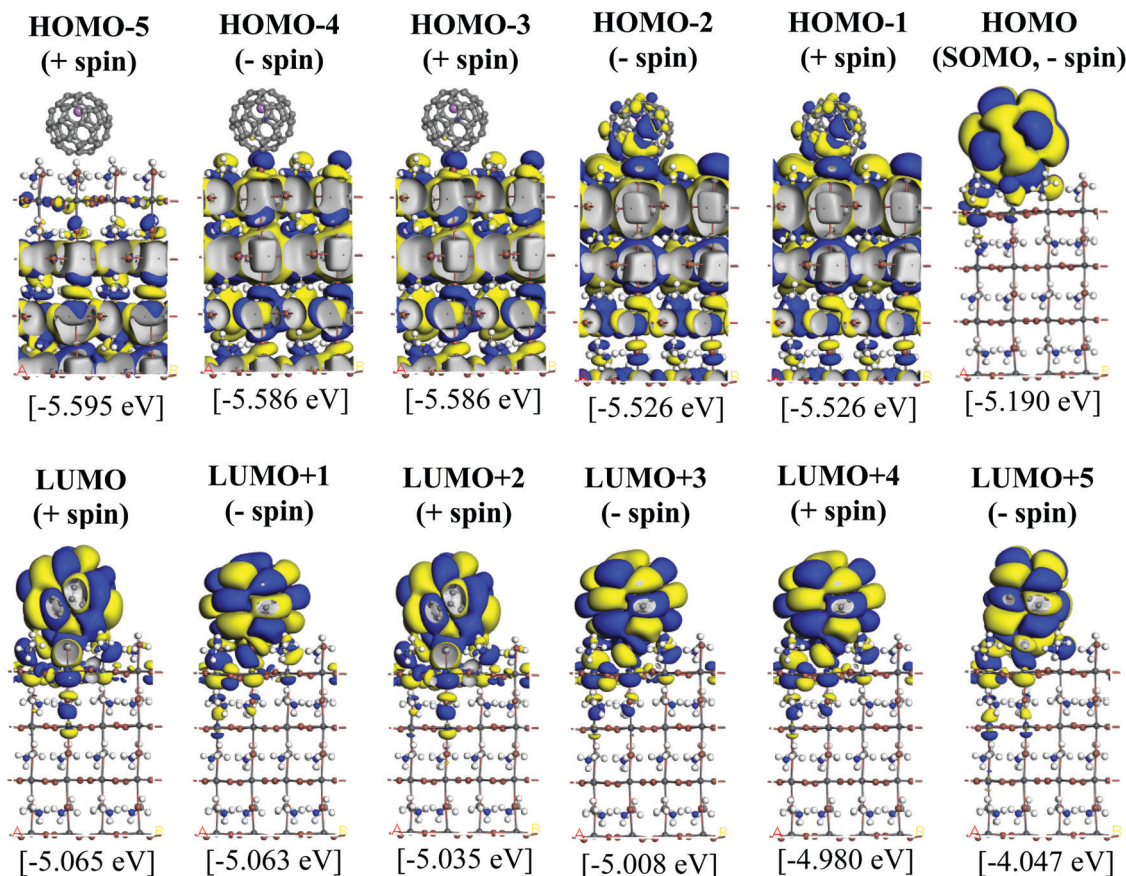


Fig. 8 Calculated KS orbitals and energy eigenvalues of a perovskite MAPbI₃ with a neutral lithium endohedral fullerene Li@C₆₀ on the aboveC position. The Li is located at the off-central top inside the C₆₀ cage. Yellow and blue denote the plus and minus regions of the orbitals.

is higher than that of the MAPbI₃/Li⁺@C₆₀ system with the bridge position, though the system with the aboveI position is more stable and possesses stronger binding energy. This is because the charge transfer of MAPbI₃ to the Li⁺@C₆₀ on the aboveI position is facilitated by the iodine, which has a high electronegativity. This was evidenced by the fragment [I1] of the aboveI geometry possessing Hirshfeld charges of $-0.169e$ to $-0.177e$, whereas fragment [I1] of the aboveC and bridge geometries have the Hirshfeld charges of $> -0.2e$. This implies that more charges are transferred by fragment [I1] in the MAPbI₃/Li⁺@C₆₀ system with the aboveI position than that of the system with the aboveC or bridge position. Since the MAPbI₃/Li@C₆₀ system is neutral, there is almost no transfer of charge $Q \sim 0e$.

Fig. 5 and 6 illustrate the Kohn–Sham (KS) orbitals and energy eigenvalues of the topC heterojunction with a Li⁺@C₆₀ on the aboveC, aboveI, and bridge positions for Li⁺ located at the off-central top and bottom inside the C₆₀ cage, respectively. From the KS orbitals and energy eigenvalues, we find that the energy gap of MAPbI₃ is between the HOMO and LUMO+3 levels and amounts to 1.6–1.7 eV. Under light illumination, electrons are excited by this energy and transferred to the ETM, then holes are produced at the HOMO and HOMO–1 levels in the HTM. If there is no other level in the wide band gap of

MAPbI₃, the created holes can promote the following reactions, similar to the case of TiO₂:⁶⁰



Inside the band gap of MAPbI₃, however, the LUMO, LUMO+1, and LUMO+2 levels are localized at Li⁺@C₆₀. The location of these levels is about 0.6 eV higher than the HOMO level (see also Table S1, ESI†). These levels reflect the situation after an electron is transferred from Li@C₆₀ to infinitely far away, and a hole is created in the system. The KS energy levels of the neutral, spin-polarized MAPbI₃/Li@C₆₀ system (before an electron is transferred from Li@C₆₀) are shown in Fig. 7 and 8, respectively, for the off-central bottom and top Li positions. The neutral Li@C₆₀ in this system may be regarded as Li⁺@C₆₀^{•-} in ref. 61. The HOMO (SOMO, - spin) and LUMO (+spin) levels are localized at Li@C₆₀, and the latter is higher than the former by 0.125 eV; see also the values in the parentheses in Table 2. This is much smaller than the energy difference (0.336 eV for top Li position and 0.476 eV for bottom Li position) between the HOMO (SOMO, - spin) and HOMO–1 (+spin) levels. Therefore, the hole can easily migrate between Li@C₆₀ molecules, not deep inside the MAPbI₃. This is a critical reason why the hole



does not directly attack the MAPbI₃ surface when Li⁺@C₆₀ exists on the surface.

Conclusions

In summary, we have performed first-principles DFT calculations on the electronic structure of MAPbI₃/Li⁺@C₆₀ heterojunctions. Finite slab models of tetragonal MAPbI₃ (001) surfaces with MAI terminations were considered. A Li⁺ (or Li) endohedral fullerene Li⁺@C₆₀ (or Li@C₆₀) was introduced at different positions on the MAPbI₃ surface. We considered the energetically most stable topC geometry of the tetragonal MAPbI₃ surface and found that the Li⁺@C₆₀ was adsorbed at the aboveC position with almost 100% ionization. There was not much difference between the top and bottom positions of Li⁺ inside C₆₀, but the bottom position was slightly more stable than the top position. In the MAPbI₃/Li⁺@C₆₀ system, the KS wave functions of the HOMO and HOMO−1 levels were spread out in MAPbI₃ and those of the LUMO, LUMO+1, LUMO+2 levels were localized in Li⁺@C₆₀; the energy gap between these levels was 0.6 eV. Thus, in the neutral, spin-polarized MAPbI₃/Li@C₆₀ system, the KS wave functions of the HOMO (SOMO, −spin) and LUMO (+spin) levels were both localized in Li@C₆₀ and their energy gap of 0.125 eV was very small. This HOMO (SOMO) level behaves as a hole level when it loses an electron to become Li⁺@C₆₀. Since there were three almost degenerate LUMO+1 and LUMO+2 levels, it was expected to behave as a good hole conductor. Due to this fact, we concluded that the use of Li⁺@C₆₀ molecules in place of the bare Li-ions as dopant materials in the MAPbI₃ solar cells can prevent degradation. In any case, regardless of the adsorption geometry, our results clearly show the existence of the energetically isolated hole level localized in the Li@C₆₀, which may successfully contribute to the suppression of the oxidation of the MAPbI₃ surface. Thus, the present study reveals the stability of the MAPbI₃ surfaces.

Conflicts of interest

There are no conflicts to declare.

Acknowledgements

This work has been supported by Institute for Materials Research, Tohoku University and Dassault Systèmes BIOVIA for the use of supercomputer facilities of IMR and for the ambassador license of BIOVIA. KHChew acknowledges the support from the UM Research Grant (No. GPF079A-2020).

References

- 1 A. Kojima, K. Teshima, Y. Shirai and T. Miyasaka, *J. Am. Chem. Soc.*, 2009, **131**, 6050.
- 2 M. M. Lee, J. Teuscher, T. Miyasaka, T. N. Murakami and H. J. Snaith, *Science*, 2012, **338**, 643.
- 3 A. K. Jena, A. Kulkarni and T. Miyasaka, *Chem. Rev.*, 2019, **119**, 3036.
- 4 X. Li, D. Bi, C. Yi, J.-D. Decoppet, J. Luo, S. M. Zakeeruddin, A. Hagfeldt and M. A. Gratzel, *Science*, 2016, **353**, 58.
- 5 N. J. Jeon, H. Na, E. H. Jung, T.-Y. Yang, Y. G. Lee, G. Kim, H. W. Shin, S. I. Seok, J. Lee and J. Seo, *Nat. Energy*, 2018, **3**, 682.
- 6 A. Y. Alsalloum, B. Turedi, X. Zheng, S. Mitra, A. A. Zhumeckenov, K. J. Lee, P. Maity, I. Gereige, A. AlSaggaf, I. S. Roqan, O. F. Mohammed and O. M. Bakr, *ACS Energy Lett.*, 2020, **5**, 657.
- 7 K.-H. Chew, R. Kuwahara and K. Ohno, *Mater. Adv.*, 2021, **2**, 1665.
- 8 Y. Fang, C. Bi, D. Wang and J. Huang, *ACS Energy Lett.*, 2017, **2**, 782.
- 9 T. Gatti, E. Menna, M. Meneghetti, M. Maggini, A. Petrozza and F. Lamberti, *Nano Energy*, 2017, **41**, 84.
- 10 J. Pascual, J. L. Delgado and R. Tena-Zaera, *J. Phys. Chem. Lett.*, 2018, **9**, 2893.
- 11 E. Castro, J. Murillo, O. Fernandez-Delgado and L. Echegoyen, *J. Mater. Chem. C*, 2018, **6**, 2635.
- 12 H.-S. Kim, C.-R. Lee, J.-H. Im, K.-B. Lee, T. Moehl, A. Marchioro, S.-J. Moon, H.-B. Robin, J.-H. Yum, J. E. Moser, M. Grätzel and N.-G. Park, *Sci. Rep.*, 2012, **2**, 591.
- 13 J. Liu, Y. Wu, C. Qin, X. Yang, T. Yasuda, A. Islam, K. Zhang, W. Peng, W. Chena and L. Han, *Energy Environ. Sci.*, 2014, **7**, 2963.
- 14 R. S. Sanchez and E. Mas-Marza, *Solar Energy Mater., Solar Cells*, 2016, **158**, 189.
- 15 F. Zhao, L. Deng, K. Wang, C. Han, Z. Liu, H. Yu, J. Li and B. Hu, *Appl. Mater. Interfaces*, 2020, **12**, 5120.
- 16 K. Domanski, J.-P. Correa-Baena, N. Mine, M. K. Nazeeruddin, A. Abate, M. Saliba, W. Tress, A. Hagfeldt and M. Grätzel, *ACS Nano*, 2016, **10**, 6306.
- 17 A. K. Jena, Y. Numata, M. Ikegami and T. Miyasaka, *J. Mater. Chem. A*, 2018, **6**, 2219.
- 18 I. Jeon, H. Ueno, S. Seo, K. Aitola, R. Nishikubo, A. Saeki, H. Okada, G. Boschloo, S. Maruyama and Y. Matsuo, *Angew. Chem.*, 2018, **57**, 4607.
- 19 S. Yun, X. Zhou, J. Even and A. Hagfeldt, *Angew. Chem., Int. Ed.*, 2017, **56**, 15806.
- 20 X. Zhou, J. Jankowska, H. Dong and O. V. Prezhdo, *J. Energy Chem.*, 2018, **27**, 637.
- 21 C.-J. Yu, *J. Phys. Energy*, 2019, **1**, 022001.
- 22 J. Yin, D. Cortecchia, A. Krishna, S. Chen, N. Mathews, A. C. Grimsdale and C. Soci, *J. Phys. Chem. Lett.*, 2015, **6**, 1396.
- 23 S. Aoyagi, E. Nishibori, H. Sawa, K. Sugimoto, M. Takata, Y. Miyata, R. Kitaura, H. Shinohara, H. Okada, T. Sakai, Y. Ono, K. Kawachi, K. Yokoo, S. Ono, K. Omote, Y. Kasama, S. Ishikawa, T. Komuro and H. Tobita, *Nat. Chem.*, 2010, **2**, 678.
- 24 K. Ohno, Y. Maruyama, K. Esfarjani, Y. Kawazoe, N. Sato, R. Hatakeyama, T. Hirata and M. Niwano, *Phys. Rev. Lett.*, 1996, **76**, 3590.
- 25 E. E. B. Campbell, R. Tellgmann, N. Krawez and I. V. Hertel, *J. Phys. Chem. Solids*, 1997, **58**, 1763.



- 26 R. Hatakeyama, *Rev. Mod. Plasma Phys.*, 2017, **1**, 7.
- 27 K. Ohno, A. Manjanath, Y. Kawazoe, R. Hatakeyama, F. Misaizu, E. Kwon, H. Fukumura, H. Ogasawara, Y. Yamada, C. Zhang, N. Sumi, T. Kamigak, K. Kawachi, K. Yokoo, S. Ono, Y. Kasama, K. Ohno, A. Manjanath, Y. Kawazoe, R. Hatakeyama, F. Misaizu, E. Kwon, H. Fukumura, H. Ogasawara, Y. Yamada, C. Zhang, N. Sumi, T. Kamigak, K. Kawachi, K. Yokoo, S. Ono and Y. Kasama, *Nanoscale*, 2018, **10**, 1825.
- 28 H. Ueno, K. Kokubo, Y. Nakamura, K. Ohkubo, N. Ikuma, H. Moriyama, S. Fukuzumi and T. Oshima, *Chem. Commun.*, 2013, **49**, 7376.
- 29 Y. Kawashima, K. Ohkubo and S. Fukuzumi, *Chem. – Asian J.*, 2015, **10**, 44.
- 30 Y. Yamada, A. V. Kuklin, S. Sato, F. Esaka, N. Sumi, C. Zhang, M. Sasaki, E. Kwon, Y. Kasama, P. V. Avramov and S. Sakai, *Carbon*, 2018, **133**, 23.
- 31 H. J. Chandler, M. Stefanou, E. E. B. Campbell and R. Schaub, *Nat. Commun.*, 2019, **10**, 2283.
- 32 K. Miwa, S. Aoyagi, T. Sasamori, H. Ueno, H. Okada and K. Ohkubo, *J. Phys. Chem. B*, 2021, **125**, 918.
- 33 H. Ando and Y. Nakao, *Phys. Chem. Chem. Phys.*, 2021, **23**, 9785.
- 34 B. Delley, *J. Chem. Phys.*, 1990, **92**, 508.
- 35 B. Delley, *J. Chem. Phys.*, 2000, **113**, 7756.
- 36 B. Delley, in *Modern density functional theory: A tool for chemistry in theoretical and computational chemistry*. ed. J. M. Seminario and P. Politzer, Elsevier, 1995, Vol. 2.
- 37 E. R. McNellis, J. Meyer and K. Reuter, *Phys. Rev. B: Condens. Matter Mater. Phys.*, 2009, **80**, 205414.
- 38 A. Tkatchenko and M. Scheffler, *Phys. Rev. Lett.*, 2009, **102**, 073005.
- 39 J. P. Perdew, K. Burke and M. Ernzerhof, *Phys. Rev. Lett.*, 1996, **77**, 3865.
- 40 W.-J. Yin, T. Shi and Y. Yan, *J. Phys. Chem. C*, 2015, **119**, 5253.
- 41 R. A. Jishi, O. B. Ta and A. A. Sharif, *J. Phys. Chem. C*, 2014, **118**, 28344.
- 42 W. Geng, L. Zhang, Y.-N. Zhang, W.-M. Lau and L.-M. Liu, *J. Phys. Chem. C*, 2014, **118**, 19565.
- 43 A. Poglitsch and D. Weber, *J. Chem. Phys.*, 1987, **87**, 6373.
- 44 Y. Kawamura, H. Mashiyama and K. Hasebe, *J. Phys. Soc. Jpn.*, 2002, **71**, 1694.
- 45 C. Quarti, F. De Angelis and D. Beljonne, *Chem. Mater.*, 2017, **29**, 958.
- 46 J. Järvi, J. Li and P. Rinke, *New J. Phys.*, 2018, **20**, 103013.
- 47 M. Wierzbowska, J. J. Melendez and D. Varsano, *Comput. Mater. Sci.*, 2018, **142**, 361.
- 48 C. Motta, F. El-Mellouhi, S. Kais, N. Tabet, F. Alharabi and S. Sanvito, *Nat. Commun.*, 2015, **6**, 7026.
- 49 V. D'Innocenzo, G. Grancini, M. J. P. Alcocer, A. R. S. Kandada, S. D. Stranks, M. M. Lee, G. Lanzani, H. J. Snaith and A. Petrozza, *Nat. Commun.*, 2014, **5**, 3586.
- 50 S. Kawai, T. Nishiuchi, T. Kodama, P. Spijker, R. Pawlak, T. Meier, J. Tracey, T. Kubo, E. Meyer and A. D. Foster, *Sci. Adv.*, 2017, **3**, e1603258.
- 51 Z. Han, G. Czap, C.-I. Chiang, C. Xu, P. J. Wagner, X. Wei, Y. Zhang, R. Wu and W. Ho, *Science*, 2017, **358**, 206.
- 52 S. Kawai, A. Sadeghi, F. Xu, L. Peng, A. Orita, J. Otera, S. Goedecker and E. Meyer, *ACS Nano*, 2015, **9**, 2574.
- 53 S. Alvarez, *Dalton Trans.*, 2013, **42**, 8617.
- 54 F. Brivio, J. M. Frost, J. M. Skelton, A. J. Jackson, O. J. Weber, M. T. Weller, A. R. Goñi, A. M. A. Leguy, P. R. F. Barnes and A. Walsh, *Phys. Rev. B: Condens. Matter Mater. Phys.*, 2015, **92**, 144308.
- 55 M. Grechko, S. A. Bretschneider, L. Vietze, H. Kim and M. Bonn, *Angew. Chem., Int. Ed.*, 2018, **57**, 13657.
- 56 K. N. Boldyrev, V. E. Anikeeva, O. I. Semenova and M. N. Popova, *J. Phys. Chem. C*, 2020, **124**, 23307.
- 57 R. Sharma, Z. Dai, L. Gao, T. M. Brenner, L. Yadgarov, J. Zhang, Y. Rakita, R. Korobko, A. M. Rappe and O. Yaffe, *Phys. Rev. Mater.*, 2020, **4**, 092401(R).
- 58 V. Siva, A. Shameem, A. Murugan, S. Athimoolam, M. Suresh and S. A. Bahadur, *Chem. Data Collect.*, 2019, **24**, 100281.
- 59 F. L. Hirshfeld, *Theor. Chim. Acta*, 1977, **44**, 129.
- 60 O. Legrini, E. Oliveros and A. M. Braun, *Chem. Rev.*, 1993, **93**, 671.
- 61 H. Okada, H. Ueno, Y. Takabayashi, T. Nakagawa, M. Vrankić, J. Arvanitidis, T. Kusamoto, K. Prassides and Y. Matsuo, *Carbon*, 2019, **153**, 467.

